

Perovskite oxides for visible-light-absorbing ferroelectric and photovoltaic materials

Ilya Grinberg¹, D. Vincent West², Maria Torres³, Gaoyang Gou¹, David M. Stein², Liyan Wu², Guannan Chen³, Eric M. Gallo³, Andrew R. Akbashev³, Peter K. Davies², Jonathan E. Spanier³ & Andrew M. Rappe¹

Ferroelectrics have recently attracted attention as a candidate class of materials for use in photovoltaic devices, and for the coupling of light absorption with other functional properties^{1–7}. In these materials, the strong inversion symmetry breaking that is due to spontaneous electric polarization promotes the desirable separation of photo-excited carriers and allows voltages higher than the bandgap, which may enable efficiencies beyond the maximum possible in a conventional p–n junction solar cell^{2,6,8–10}. Ferroelectric oxides are also stable in a wide range of mechanical, chemical and thermal conditions and can be fabricated using low-cost methods such as sol–gel thin-film deposition and sputtering^{3,5}. Recent work^{3,5,11} has shown how a decrease in ferroelectric layer thickness and judicious engineering of domain structures and ferroelectric–electrode interfaces can greatly increase the current harvested from ferroelectric absorber materials, increasing the power conversion efficiency from about 10^{-4} to about 0.5 per cent. Further improvements in photovoltaic efficiency have been inhibited by the wide bandgaps (2.7–4 electronvolts) of ferroelectric oxides, which allow the use of only 8–20 per cent of the solar spectrum. Here we describe a family of single-phase solid oxide solutions made from low-cost and non-toxic elements using conventional solid-state methods: $[\text{KNbO}_3]_{1-x}[\text{BaNi}_{1/2}\text{Nb}_{1/2}\text{O}_3-\delta]_x$ (KBNNO). These oxides exhibit both ferroelectricity and a wide variation of direct bandgaps in the range 1.1–3.8 electronvolts. In particular, the $x = 0.1$ composition is polar at room temperature, has a direct bandgap of 1.39 electronvolts and has a photocurrent density approximately 50 times larger than that of the classic ferroelectric (Pb,La)(Zr,Ti)O₃ material. The ability of KBNNO to absorb three to six times more solar energy than the current ferroelectric materials suggests a route to viable ferroelectric semiconductor-based cells for solar energy conversion and other applications.

The wide bandgap of typical ferroelectric perovskites (with ABO₃ composition) is due to the fundamental characteristics of the metal–oxygen A–O and B–O bonds. The excitation across the bandgap is essentially a charge transfer from the oxygen (O) 2p states at the valence band maximum to the transition-metal d states at the conduction band minimum. Transition-metal B cations enable the perovskite oxide to exhibit ferroelectricity¹². Owing to a large difference in electronegativity between the oxygen and transition-metal atoms, the bandgap is quite large (3–5 eV). The lowest known bandgap for a ferroelectric oxide has been $E_g = 2.7$ eV, obtained for BiFeO₃ and the recently fabricated LaCoO₃-doped Bi₄Ti₃O₁₂ films^{6,13}. This made BiFeO₃ the subject of a number of investigations for photovoltaic applications^{1,4,14}. However, BiFeO₃ is capable of absorbing only 20% of the solar spectrum, necessitating the development of new semiconducting ferroelectric oxides. For example, a weakly ferroelectric non-perovskite KBiFe₂O₅ material has recently been discovered with a bandgap of 1.6 eV (ref. 15).

Following the bandgap-engineering strategy explored in a previous theoretical study^{16–18} on Ni-doped PbTiO₃, we used two different transition-metal cations on the perovskite B-site to create ferroelectric

perovskites with low bandgaps, with one cation driving ferroelectricity and the other giving an E_g in the visible range. We used the classic ferroelectric perovskite KNbO₃ (KNO) to provide off-centre distortions and polarization ($P \approx 0.55$ C m⁻² at 0 K)¹⁹, and mix it with BaNi_{1/2}Nb_{1/2}O₃ – δ (BNNO) to introduce a combination of Ni²⁺ on the B-site and an oxygen vacancy, which can give rise to electronic states in the gap of the parent KNO material. Nb-containing ferroelectric perovskites have been shown to tolerate a high concentration of vacancies²⁰ so B-site Nb ions should be able to accommodate the Ni²⁺–oxygen vacancy combination. The large sizes of K and Ba cations favour solubility and vacancy formation, because Ni³⁺ has a small ionic radius and is only stable in perovskites with (small) La³⁺ cations on the A-site, whereas the larger Ni²⁺ ion is known to be stable in ferroelectric compounds such as PbNi_{1/3}Nb_{2/3}O₃ (ref. 21).

The solid solutions $[\text{KNbO}_3]_{1-x}[\text{BaNi}_{1/2}\text{Nb}_{1/2}\text{O}_3-\delta]_x$ with compositions $x = 0.1$ –0.5 were synthesized by standard solid-state synthesis methods. The samples were sintered to 95% density and characterized. Synchrotron X-ray diffraction shows (Fig. 1b) the formation of a stable perovskite for all solutions, with very small NiO impurity peaks. The increase in lattice parameters with BNNO substitution is consistent with the presence of the Ni²⁺ cation, with a larger ionic radius (0.69 Å) than Nb⁵⁺ (0.64 Å) or Ni³⁺ (0.60 Å).

To examine the microscopic structure and properties of KBNNO, we performed first-principles density functional theory (DFT) calculations for the $x = 0.33$ composition using a 60-atom supercell (Fig. 1c). Two of the twelve Nb⁵⁺ ions are replaced by Ni²⁺, and four of the twelve K ions are replaced by Ba. This substitution will generate an oxygen vacancy $V_O^{\bullet\bullet}$ adjacent to Ni_{Nb}^{''} defects (in Kröger–Vink notation)²² with the local dipole (Ni–V_O) parallel to the overall polarization P . We obtained two stable KBNNO configurations, with the local structure of Ni²⁺–V_O–Ni²⁺ and Ni²⁺–V_O–Nb⁵⁺ (Fig. 1c). The calculated P values are 0.19 C m⁻² and 0.18 C m⁻² for the two KBNNO structures, mainly owing to the Nb off-centre distortions. The polarization is smaller than that of the parent KNO material ($P = 0.43$ C m⁻² at 0 K in DFT) but still substantial. Comparison of lattice parameters for fully oxidized ($\delta = 0$) compositions (KBNNO_{ox}) and KBNNO ($\delta > 0$, with oxygen vacancies) showed that KBNNO volume is increased compared to KNO, in agreement with experimental data, whereas the KBNNO_{ox} volume is decreased (Extended Data Table 1). At the synthesis conditions, DFT + U (where U is the Hubbard on-site repulsion term) free-energy calculations²³ found oxygen vacancies to be thermodynamically favoured, indicating that the material is in the KBNNO state. Finally, KBNNO samples are not conductive, in contrast to KBNNO_{ox}, for which the DFT + U calculations predict a metallic state. Therefore, the material we synthesized is indeed KBNNO, with oxygen vacancies.

For efficient and practical separation of excited carriers, ferroelectrics must be polar at room temperature and higher. Comparison of the 0–K, DFT-calculated P values for KNO and $x = 0.33$ KBNNO (0.43 C m⁻² and about 0.2 C m⁻², respectively) shows that BNNO substitution decreases polarization. This should reduce the temperature

¹The Makineni Theoretical Laboratories, Department of Chemistry, University of Pennsylvania, Philadelphia, Pennsylvania 19104-6323, USA. ²Department of Materials Science and Engineering, University of Pennsylvania, Philadelphia, Pennsylvania 19104-6272, USA. ³Department of Materials Science and Engineering, Drexel University, Philadelphia, Pennsylvania 19104, USA.

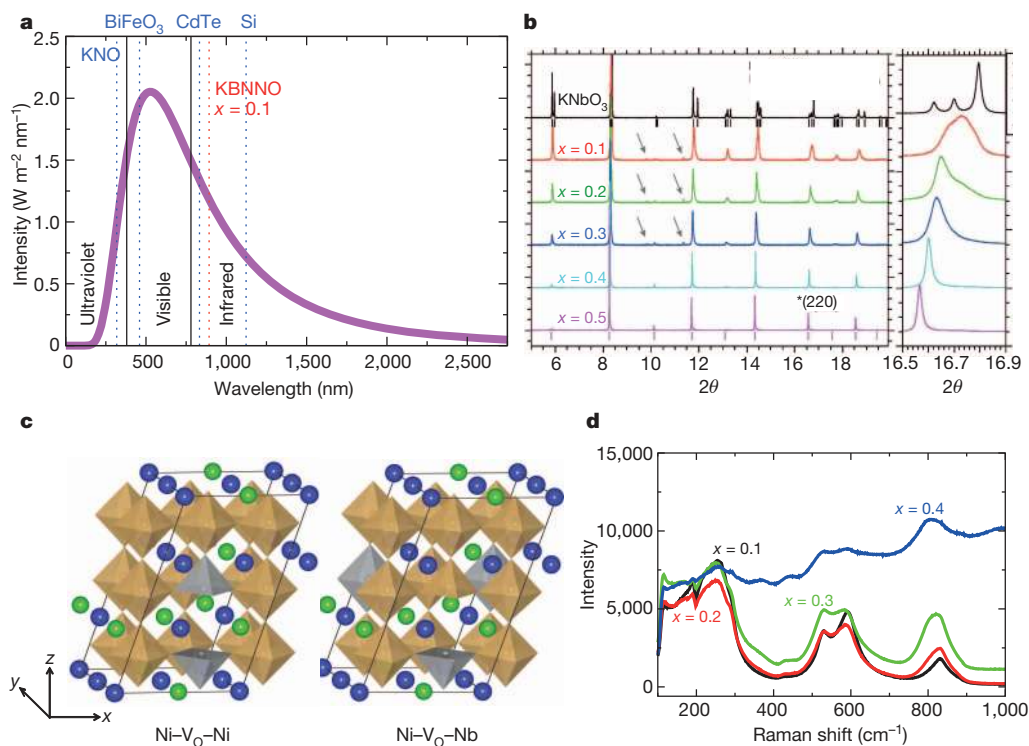


Figure 1 | KBNNO structural properties. **a**, The solar spectrum and E_g values for Si, CdTe, BiFeO₃ and $x = 0.1$ KBNNO. **b**, KBNNO synchrotron X-ray diffraction results. The inset shows the $(220)_p$ family of reflections. Perovskite peaks are marked by tick marks and NiO impurity peaks by arrows. **c**, $(\text{KNbO}_3)_8-(\text{BaNb}_{1/2}\text{Ni}_{1/2}\text{O}_{2.75})_4$ crystal structures used in DFT calculations.

of the ferroelectric-to-paraelectric and orthorhombic-to-tetragonal transitions and make the tetragonal phase preferred for ferroelectric KBNNO compositions at room temperature²⁴. X-ray-diffraction data for the $(220)_p$ (where ‘p’ represents the cubic perovskite sub-cell) peak for $x = 0-0.5$ compositions shows a gradual transition from the orthorhombic ferroelectric KNO structure to a cubic structure at $x = 0.4$. For $x = 0.1$, the broad $(220)_p$ peak exhibits a shoulder on the side of lower 2θ (scattering angle); this is consistent with a weakly tetragonal ferroelectric phase. Raman spectroscopy (Fig. 1d) shows a resonance depth at 200 cm^{-1} and a peak at 820 cm^{-1} for $x \leq 0.3$ compositions; these have been identified as signatures of ferroelectricity in KNbO_3 -based solid solutions²⁵. These features are sharpest for the $x = 0.1$ composition, which also exhibits peaks in the dielectric constant at around 450 K and at around 600 K (Extended Data Fig. 1a) and is the focus of our further investigation.

The ferroelectric switching measurements on a $20\text{-}\mu\text{m}$ -thick $x = 0.1$ sample in high vacuum (pressure of 10^{-7} torr) at 77–170 K showed standard ferroelectric hysteresis loops reaching the maximum value of about 0.2 C m^{-2} at 170 K (Fig. 2a, Extended Fig. 1b) for an applied field of 250 kV cm^{-1} . We ascribe the increase of measured P with temperature to the greater speed of domain-wall motion and, therefore, more effective switching at higher temperatures. The measured P value is therefore the lower limit of the true bulk P . With further increase in temperature, increased leakage made poling ineffective. Under ambient conditions, poling of the sample produced very thin, elongated loops with P reaching only 0.01 C m^{-2} (Extended Data Fig. 1c, d). In contrast to the hysteresis measurements at room temperature (300 K), local ferroelectric piezoelectric measurements on a thin and electrically addressable lamella extracted (see Methods) from an $x = 0.1$ sample (Fig. 2b) showed a strong switching loop characteristic of ferroelectric materials, as has been found before for leaky ferroelectrics^{1,15}. Taken together, the DFT calculations and experimental data unambiguously show the presence of strong P in KBNNO for $x = 0.1$.

K and Ba are shown by blue and green spheres, respectively; Nb–O₆ and Ni–O₆ are shown as brown and grey octahedra with O atoms at the vertices. **d**, Raman data for KBNNO $x = 0.1-0.4$ compositions. For $x \leq 0.3$, a depth resonance at 200 cm^{-1} and a peak near 800 cm^{-1} indicate a ferroelectric phase²⁵.

We characterize the light-absorption properties of the KBNNO pellets using spectroscopic ellipsometry (Fig. 2c). We find that the bandgaps of Ni-containing KBNNO solutions are in the range 1.1–2.0 eV; this is much lower than the 3.8-eV bandgap of the KNO material (Fig. 2d). Owing to the smaller bandgap, the samples are green, in contrast to KNO, which is white. The bandgap tunability of 2.7 eV is 150% greater than previously achieved by doping of ferroelectric $\text{Bi}_4\text{Ti}_3\text{O}_{12}$ or by the doping of the non-ferroelectric perovskite $\text{Ba}(\text{In}_{1/2}\text{Ta}_{1/2})\text{O}_3$ and is on par with the largest bandgap tunabilities observed in oxides (such as $E_g = 1.4-3.9 \text{ eV}$ variation in $\text{CdO}-\text{CaO}$ solid solutions)^{6,26-28}. To our knowledge, the $E_g = 1.1-3.8 \text{ eV}$ variation of KBNNO solid solutions is the largest ever observed for a perovskite or a ferroelectric material. The bandgaps are direct, as indicated by a single slope of the extinction coefficient versus wavelength, and the power law of its variation. The absorption coefficient is approximately $2.5 \times 10^4 \text{ cm}^{-1}$ at 885 nm, comparable to the absorption coefficient of CdTe and GaAs. Inspection of Fig. 2d shows that there is a non-monotonic change in E_g with BNNO fraction, with an initial steep decay for low BNNO fraction and then a slow rise starting from $x = 0.3$.

To elucidate the origin of the bandgap lowering in the KBNNO solid solutions, we examined the electronic structure of KBNNO with first-principles methods. The electronic structures of the $x = 0.33$ KBNNO supercells show direct bandgaps of 1.84 eV and 1.49 eV, much smaller than the 2.3-eV local density approximation (LDA) + U bandgap of KNO (Extended Data Fig. 2). The valence band maximum consists of hybridized Ni 3d and O 2p states, while the conduction band minimum is composed of Nb 4d states. The filled Ni 3d gap states in KBNNO therefore play a crucial part in lowering the bandgap.

Photoresponse measurements showed that KBNNO is promising for photovoltaic applications. We first examined the dependence of the photocurrent response of KBNNO on incident optical wavelength, using a monochromatic source tunable from 700 to 900 nm (Fig. 3a).

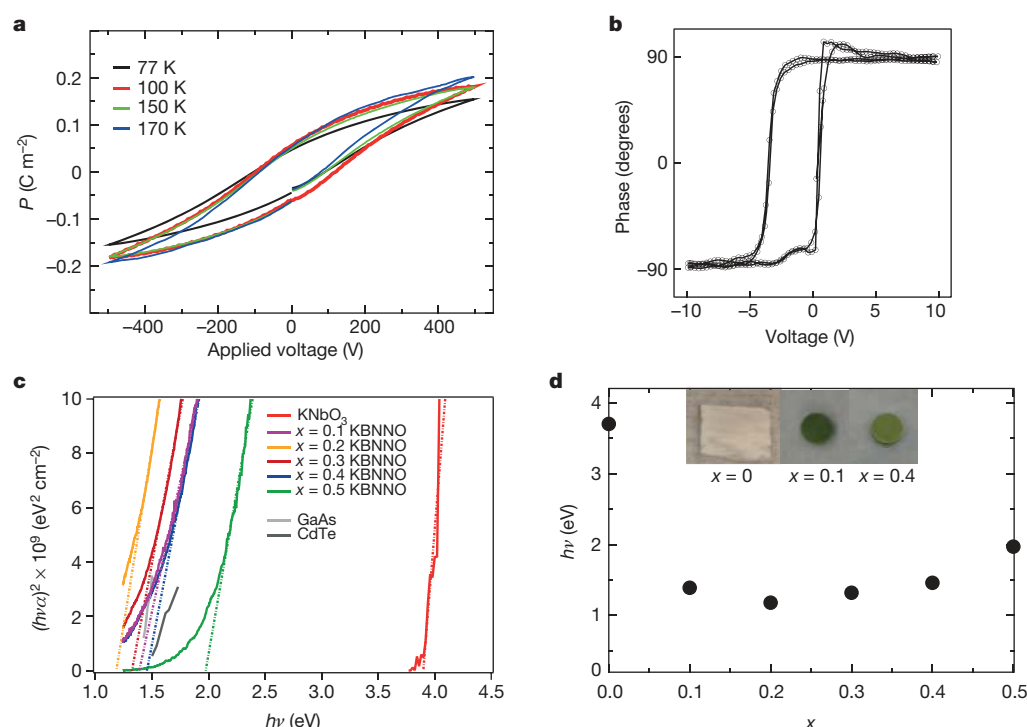


Figure 2 | Experimental results for ferroelectricity and bandgap in KBNNO. **a**, Ferroelectric hysteresis loops for a 20-μm-thick $x = 0.1$ KBNNO film at 10⁻⁷ torr and 77–170 K. **b**, Local ferroelectric piezoelectric hysteresis loops measured for an $x = 0.1$ lamella sample of KBNNO. **c**, Ellipsometry measurements for KBNNO oxides with $x = 0.0$ –0.5, showing bandgaps from 1.18 eV to 3.8 eV. This makes KBNNO promising for visible solar light absorption. **d**, Bandgap values versus BNNO fraction. Also shown are images of the KNbO₃ and KBNNO pellets for $x = 0.1$ and $x = 0.4$ compositions.

The response starts to rise at about 850 nm (1.46 eV) and peaks at about 710 nm (1.74 eV), showing a good match with the solar spectrum. Measurements of the open-circuit photovoltage V_{oc} and short-circuit

photocurrent J_{sc} found that the photoresponse of KBNNO is controlled by the polarization and is much larger than that for the classic ferroelectric (Pb,Li)(Zr,Ti)O₃ and (Na,K)NbO₃ materials. The 20-μm-thick ceramic sample was first poled at 77 K with a 500 V pulse for 400 s, and its response was then measured in the dark and under illumination by a halogen lamp delivering about 4 mW cm⁻² of above-bandgap illumination (Fig. 3b). The direction of the photocurrent is reversed after the material is poled in the opposite direction; this is a signature of excited carrier separation by the bulk of material exhibited by ferroelectrics. The measured J_{sc} and V_{oc} are about 40 nA cm⁻² and 3.5 V, respectively. The large value of V_{oc} is in line with previous reports of above-bandgap photovoltage in ferroelectric materials²⁹.

We then measured V_{oc} and J_{sc} at room temperature after poling with a ± 80 -V pulse for 300 s. We note that, on the basis of the hysteresis-loop measurements discussed above, this procedure will pole only a small fraction of the sample. We found V_{oc} and J_{sc} of 0.7 mV and about 0.1 μA cm⁻², respectively. Here too, we found a reversal of photocurrent direction on change in the sign of the poling voltage (Extended Data Fig. 3). Despite the weak poling at room temperature, the 300-K J_{sc} is greater than the 77-K J_{sc} . This is due to the strong dependence of J_{sc} on temperature²⁹. The room-temperature J_{sc} is higher than 8 nA cm⁻² for a 50-μm (Pb,Li)(Zr,Ti)O₃ sample or 25 nA cm⁻² for 0.84-μm (Na,K)NbO₃ samples measured in previous 300-K experiments under ultraviolet illumination^{30,31}. Our 300-K KBNNO results also compare favourably to the photoresponse of BiFeO₃ reported¹ for a 70-μm sample under green-light illumination ($J_{sc} = 4$ μA cm⁻², $V_{oc} = 35$ mV for 10 mW cm⁻² illumination) considering the broad-spectrum illumination and the partial poling for our KBNNO sample.

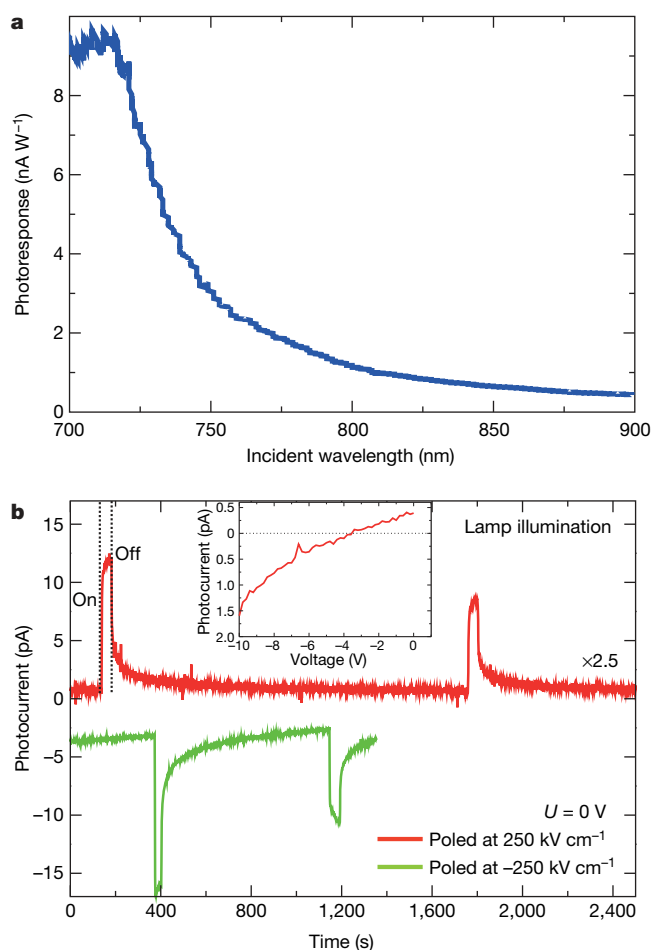


Figure 3 | Photocurrent measurements for the KBNNO samples. **a**, The current collected between two co-planar 85-μm² electrodes per watt of total incident illumination. The photoresponse starts at the bandgap energy of 1.39 eV and saturates at 1.74 eV. **b**, Ferroelectric photovoltaic effect under short circuit ($U = 0$) conditions for 20-μm-thick $x = 0.1$ film at 77 K following poling by a ± 500 -V pulse applied for 400 s and under 4 mW cm⁻² of above-bandgap illumination. Reversal of poling voltage results in the reversal of photocurrent direction. The inset shows the photoresponse versus applied bias at 77 K obtained by subtracting light current from dark; a large V_{oc} of 3.5 V is observed.

Decreased thickness of the ferroelectric layer and optimization of the ferroelectric–metal interfaces have been shown to increase the photocurrent of wide-bandgap ferroelectric-based solar cells by up to six orders of magnitude^{3,5}. In particular, 270-nm-thick PZT-based cells with a Cu₂O cathode buffer layer have been demonstrated to reach a tenth of the theoretically possible efficiency (0.57% for the case of PZT with $E_g = 3.5$ eV.) The ideal match of the KBNNO bandgap to the solar spectrum, its compositional tuning throughout the visible range and its photoresponse properties open up the possibility of ferroelectric photovoltaic efficiency of >3% in a thin-film device and the use of ferroelectric materials as solar absorber layers and carrier separators in practical photovoltaics. It is also important for the emerging field of ferroelectric photovoltaics as the first visible-light-absorbing strongly ferroelectric material.

METHODS SUMMARY

All samples were made by standard solid-state synthesis techniques in the powder form, followed by sintering. An integrated focused ion beam and scanning electron microscope (FEI, DB235) equipped with a lift-out tool (Omniprobe) was used to extract thin-film lamellae from the bulk-synthesized KBNNO pellets for bandgap and local ferroelectric piezoelectric switching measurements. Mesoscopic (about 20 μm thick) samples were prepared by metallization of the polished side of each pellet using thermally evaporated layers of Cr (5 nm) and Au (100 nm), followed by mounting with the pellet's metallized side face down, thinning and subsequent polishing to a root mean squared roughness of around 100 nm. Indium/tin oxide thin films (about 50 nm) were subsequently deposited onto shadow-masked, approximately 20- μm -thick KBNNO via pulsed laser deposition at 200 °C in O₂. Bandgaps were measured by spectroscopic ellipsometry using a variable-angle spectroscopic ellipsometer equipped with Glan–Taylor polarizers, a rotating compensator, and deuterium and quartz halogen lamps for spectral coverage (J. A. Woollam, Model M2000). Ferroelectric switching within the lamellae was evaluated from the local piezoresponse using a scanning probe microscope (Asylum Research, MFP-3D) and Pt-coated Si probes (Olympus, AC 240TM; nominal stiffness constant, about 2 N m⁻¹). Ferroelectric polarization hysteresis measurements were collected at 77–200 K in high vacuum (10⁻⁷ torr) and at ambient pressure using a ferroelectric tester (Radiant LC). Steady-state photocurrent/bias-voltage traces were collected in bulk KBNNO and BTO and in approximately 20- μm -thick films under 120-W tungsten–halogen spectrally broad lamp probe illumination and using a fibre-coupled supercontinuum source (NKT Compact), under vacuum (10⁻⁶ torr, Lakeshore Cryotronics, TTP4) using a picoammeter (Keithley, model 6487). Photocurrent spectra were collected using a tunable-wavelength Ti:sapphire laser (M2 SolsTiS) with an incident spot diameter of about 10 mm. First-principles DFT LDA + *U* calculations were done using norm-conserving pseudopotentials and a plane-wave basis set, as implemented in the Quantum-Espresso package.

Online Content Any additional Methods, Extended Data display items and Source Data are available in the online version of the paper; references unique to these sections appear only in the online paper.

Received 11 April; accepted 28 August 2013.

Published online 10 November 2013.

- Choi, T., Lee, S., Choi, Y., Kiryukhin, V. & Cheong, S.-W. Switchable ferroelectric diode and photovoltaic effect in BiFeO₃. *Science* **324**, 63–66 (2009).
- Yang, S. Y. *et al.* Above-bandgap voltages from ferroelectric photovoltaic devices. *Nature Nanotechnol.* **5**, 143–147 (2010).
- Cao, D. *et al.* High-efficiency ferroelectric-film solar cells with an n-type Cu₂O cathode buffer layer. *Nano Lett.* **12**, 2803–2809 (2012).
- Alexe, M. & Hesse, D. Tip-enhanced photovoltaic effects in bismuth ferrite. *Nature Commun.* **2**, 256 (2011).
- Qin, M., Ao, K. & Liang, Y. C. High efficiency photovoltaics in nanoscaled ferroelectric thin films. *Appl. Phys. Lett.* **93**, 122904 (2008).
- Choi, W. S. *et al.* Wide bandgap tunability in complex transition metal oxides by site-specific substitution. *Nature Commun.* **3**, 689 (2012).
- Kreisel, J., Alexe, M. & Thomas, P. A. A photoferroelectric material is more than the sum of its parts. *Nature Mater.* **11**, 260 (2012).
- Fridkin, V. M. *Photoferroelectrics* (Springer, 1979).
- Inoue, Y., Sato, K., Sato, K. & Miyama, H. Photoassisted water decomposition by ferroelectric lead zirconate titanate ceramics with anomalous photovoltaic effects. *J. Phys. Chem.* **90**, 2809–2810 (1986).
- Young, S. M. & Rappe, A. M. First principles calculation of the shift current photovoltaic effect in ferroelectrics. *Phys. Rev. Lett.* **109**, 116601 (2012).

- Glass, A. M., Linde, D. V. D. & Negran, T. J. High-voltage bulk photovoltaic effect and photorefractive process in LiNbO₃. *Appl. Phys. Lett.* **25**, 233–235 (1974).
- Cohen, R. E. Origin of ferroelectricity in perovskite oxides. *Nature* **358**, 136–138 (1992).
- Basu, S. R. *et al.* Photoconductivity in BiFeO₃ thin films. *Appl. Phys. Lett.* **92**, 091905 (2008).
- Yang, S. Y. *et al.* Photovoltaic effects in BiFeO₃. *Appl. Phys. Lett.* **95**, 062909 (2009).
- Zhang, G. *et al.* New high *T_c* multiferroics KBiFe₂O₅ with narrow band gap and promising photovoltaic effect. *Sci. Rep.* **3**, 1265 (2013).
- Bennett, J. W., Grinberg, I. & Rappe, A. M. New highly polar semiconductor ferroelectrics through d⁸ cation–O vacancy substitution into PbTiO₃: a theoretical study. *J. Am. Chem. Soc.* **130**, 17409–17412 (2008).
- Gou, G. Y., Bennett, J. W., Takenaka, H. & Rappe, A. M. Post density functional theoretical studies of highly polar semiconducting Pb(Ti_{1-x}Ni_x)O_{3-x} solid solutions: effects of cation arrangement on band gap. *Phys. Rev. B* **83**, 205115 (2011).
- Qi, T., Grinberg, I. & Rappe, A. M. Band-gap engineering via local environment in complex oxides. *Phys. Rev. B* **83**, 224108 (2011).
- Liang, L., Li, Y. L., Chen, L.-Q., Hu, S. Y. & Lu, G.-H. A thermodynamic free energy function for potassium niobate. *Appl. Phys. Lett.* **94**, 072904 (2009).
- Zhao, X., Qu, W. & Tan, X. Zr-modified Pb(Mg_{1/3}Nb_{2/3})O₃ with a long-range cation order. *J. Am. Ceram. Soc.* **91**, 3031–3038 (2008).
- Kondo, M. & Kurihara, K. Sintering behavior and surface microstructure of PbO-rich Pb(Ni_{1/3}Nb_{2/3})O₃–PbZrO₃ ceramics. *J. Am. Ceram. Soc.* **84**, 2469–2474 (2001).
- Kröger, F. A. & Vink, H. J. Relations between the concentrations of imperfections in crystalline solids. **3**, 307–435 (1956).
- Reuter, K. & Scheffler, M. First-principles atomistic thermodynamics for oxidation catalysis: surface phase diagrams and catalytically interesting regions. *Phys. Rev. Lett.* **90**, 046103 (2003).
- Grinberg, I. & Rappe, A. M. Local structure and macroscopic properties in Pb(Zn_{1/3}Nb_{2/3})O₃–PbTiO₃ and Pb(Mg_{1/3}Nb_{2/3})O₃–PbTiO₃ solid solutions. *Phys. Rev. B* **70**, 220101 (2004).
- Bartasyte, A., Kreisel, J., Peng, W. & Guilloux-Viry, M. Temperature-dependent Raman scattering of KTa_{1-x}Nb_xO₃ thin films. *Appl. Phys. Lett.* **96**, 262903 (2010).
- Srihari, V. *et al.* Wide band gap tunability of bulk Cd_{1-x}Ca_xO. *J. Appl. Phys.* **109**, 013510 (2011).
- Ji, S. M., Choi, S. H., Jang, J. S., Kim, E. S. & Lee, J. S. Band gap tailored Zn(Nb_{1-x}V_xO₆) solid solutions as visible light photocatalysts. *J. Phys. Chem. C* **113**, 17824–17830 (2009).
- Kim, T. W. *et al.* Substitution effect of pentavalent bismuth ions on electronic structure and physicochemical properties of perovskite-structured Ba(In_{0.5}Ta_{0.5})O₃ semiconductors. *Mater. Res. Bull.* **42**, 1914–1920 (2007).
- Brody, P. S. Temperature dependence of the short circuit photocurrent in ferroelectric ceramics. *Ferroelectrics* **10**, 143–146 (1976).
- Poosanaas, P., Dogan, A., Thakoor, S. & Uchino, K. Influence of sample thickness on the performance of photostrictive ceramics. *J. Appl. Phys.* **84**, 1508–1512 (1998).
- Park, J., Won, S. S., Ahn, C. W. & Kim, I. W. Ferroelectric photocurrent effect in polycrystalline lead-free (K_{0.5}Na_{0.5})(Mn_{0.005}Nb_{0.995})O₃ thin film. *J. Am. Ceram. Soc.* **96**, 146–150 (2013).

Acknowledgements Members of the Davies group—D.V.W., D.M.S., L.W. and P.K.D.—were supported by the Energy Commercialization Institute of BFTP. We also thank M. R. Suchomel for assistance with collection of the synchrotron X-ray data. Use of the Advanced Photon Source at Argonne National Laboratory was supported by the US Department of Energy, Office of Basic Sciences, under contract number DE-AC02-06CH11357. Members of the Spanier group—M.T. and J.E.S.—were supported by the Army Research Office, under grant number W911NF-08-1-0067. G.C. was supported by NSF grant DMR 0907381. A.R.A. was supported by the Energy Commercialization Institute of BFTP and by NSF grant DMR 1124696. E.M.G. was supported by an ASEE Postdoctoral Fellowship. Support for instrumentation used in this project was provided by the ARO DURIP programme and the NSF under grant DMR 0722845. J.E.S. also acknowledges C. L. Schauer for permitting access to the spectroscopic ellipsometer and the Drexel Centralized Research Facilities for access to instrumentation. We thank F. Yan, M. A. Islam and C. L. Johnson for assistance in transparent electrode thin-film deposition, Raman scattering, and sample thinning and polishing, respectively. Of the Rappe group, I.G. was supported by the Department of Energy, Office of Basic Energy Sciences, under grant number DE-FG02-07ER46431, G.G. was supported by the Energy Commercialization Institute and A.M.R. was supported by the Office of Naval Research, under grant number N00014-12-1-1033. Computational support was provided by a Challenge Grant from the High Performance Computing Modernization Office of the US Department of Defense and the National Energy Research Scientific Computing Center of the US Department of Energy.

Author Contributions I.G. and A.M.R. created the materials design strategy. D.V.W. and P.K.D. suggested the KBNNO composition. I.G., J.E.S., P.K.D. and A.M.R. designed the calculations and experiments and supervised the analysis of obtained results. D.V.W., D.M.S. and L.W. synthesized the KBNNO powders and pellets. D.V.W. obtained the X-ray diffraction and dielectric data. G.C. developed the procedure to prepare the lamellae from the pellets. M.T. performed the piezoresponse and ellipsometry measurements. A.R.A. and J.E.S. analysed the Raman spectra. A.R.A., G.C., E.M.G. and J.E.S. carried out the ferroelectric, photoresponse and photovoltaic measurements. G.G. performed the DFT calculations. I.G., G.G., J.E.S., A.M.R. and P.K.D. co-wrote the paper.

Author Information Reprints and permissions information is available at www.nature.com/reprints. The authors declare no competing financial interests. Readers are welcome to comment on the online version of the paper. Correspondence and requests for materials should be addressed to A.M.R. (rappe@sas.upenn.edu).

METHODS

Synthesis and dielectric measurements. All samples were made from stoichiometric quantities of dried K_2CO_3 , BaCO_3 , NiO and Nb_2O_5 powders. After mixing in a mortar, the powders were ball-milled using yttria-stabilized zirconia planetary milling media in ethanol for 2 h. The dried powders were calcined on Pt foil in an alumina crucible at 900°C for 12 h. Approximately 300 mg aliquots were pressed into 0.25-ml pellets in a uniaxial press and isostatically pressed at 80,000 psi (pounds per square inch). The pellets were placed on Pt foil in a covered alumina crucible, surrounded by sacrificial powder of the same composition to inhibit volatilization of potassium, and sintered at temperatures between $1,050^\circ\text{C}$ and $1,250^\circ\text{C}$, depending on the composition. To minimize any absorption of H_2O , which is a potential issue in the synthesis of KBNbO_3 , at all stages of the synthesis samples were kept either at elevated temperature (at least 200°C) or in a desiccator to minimize their exposure to moisture. Powder X-ray-diffraction patterns of the samples were collected on a laboratory X-ray diffractometer (Rigaku GiegerFlex D/Max-B) using $\text{Cu K}\alpha$ radiation generated at 45 kV and 30 mA and by synchrotron X-ray diffraction (wavelength 0.413473 \AA) using the Advanced Photon Source at Argonne National Laboratory. The dielectric data were collected on pellets coated with Ag paint (Heraeus ST1601-14 type) to provide electrical contacts for the Pt lead wires. The dielectric properties were investigated as functions of frequency and temperature using a high-precision impedance-capacitance-resistance meter (Hewlett-Packard, model 4284A) and a high-temperature thermal chamber. The sample temperature was monitored by an S-type thermocouple positioned near the pellet.

Spectroscopic ellipsometry. Spectroscopic ellipsometry was performed on polished KBNNO at 300 K in the 247–1,000-nm wavelength range using a variable-angle spectroscopic ellipsometer equipped with Glan–Taylor polarizers, a rotating compensator, and deuterium and quartz halogen lamps for spectral coverage (J. A. Woollam, model M2000). Measurement of the components of linearly polarized reflectivity at each selected wavelength were used to obtain the ellipsometric parameters Ψ and Δ through the relation

$$\tan\Psi(\lambda)\exp(i\Delta(\lambda)) = R_p(\lambda)/R_s(\lambda)$$

where $R_p(\lambda)$ and $R_s(\lambda)$ are reflection coefficients for light polarization parallel and perpendicular to the plane of incidence, respectively. The energy-dependent complex dielectric function was calculated using Fresnel's equations. The bandgap was calculated using a Tauc plot of $(h\nu\alpha)^2$ versus $h\nu$, where α is the absorption coefficient. Measurements were taken at 65° .

Extraction of thin-film lamellae. An integrated focused ion beam and scanning electron microscope (FEI, DB235) equipped with a lift-out tool (Omniprobe) was used to extract thin-film lamellae from the bulk-synthesized KBNNO. Briefly, a thin layer of carbon by sputtering coating (several tens of nanometres) is first deposited to provide protection against subsequent ion-beam irradiation and to enhance the imaging contrast. This was followed by deposition of a 500-nm-thick platinum film using ion-beam-assisted deposition onto the lift-out area, preventing direct ion-beam damage during the process. The lift-out preparation process consists of initial cross-sectional milling steps on both sides, a series of thinning steps using lower ion-beam currents, a finer-scale cross-sectional cleaning using an approximately 100-pA ion-beam current, and ion-beam local deposition of Pt to affix the lamella to the lift-out tool. A low beam current ($<100 \text{ pA}$) was maintained during the final release of the lamella from the substrate. Using the lift-out probe, each harvested lamella was transferred carefully to glass substrates coated with layers of fluorine-doped tin oxide (TEC-15, Pilkington) and a top coating of 30 nm of indium (selected to facilitate wetting of the bottom contact to the lamella) deposited via electron-beam evaporation in vacuum. Each lamella is transferred to the substrate with the lamella first making contact with the substrate along one edge; the free-standing lamella is then pushed down onto the surface. As a final step in the transfer of the lamellar thin-film test specimen, Pt is deposited using electron-beam-assisted deposition onto the corners of each lamella to anchor it. Following this, post-processing steps of ultralow-beam-current surface ion milling and subsequent thermal annealing (500°C for 5 h, followed by a slow cooling at 1°C s^{-1}) were carried out in a furnace (Ney Vulcan 3-130) to effectively eliminate ion damage.

Local ferroelectric measurements. The KBNNO pellets were cut to roughly $250 \mu\text{m}$ with a diamond saw and polished under water to thicknesses of about $25 \mu\text{m}$ using lapping films (3M) coated with successively finer aluminium oxide particles. The final polish was done using a slurry of $0.05\text{-}\mu\text{m}$ colloidal silica (Ted Pella) in an alkaline suspension (pH 9.8). We estimate that the surface roughness should be less than $0.1 \mu\text{m}$.

Ferroelectric switching within the lamellae was evaluated from the local piezo-response using a scanning probe microscope (Asylum Research MFP-3D) and Pt-coated Si probes (AC 240TM, Olympus; nominal stiffness constant, about 2 N m^{-1}). A triangular waveform (frequency 0.025 Hz , peak-to-peak bias of 10 V) was applied to the bottom electrode while a sinusoidal alternating-current probing voltage (5 kHz , 0.5 V amplitude) was applied to the cantilever tip to collect the variation in the cantilever phase as a function of the bias voltage. The cantilever phase signal at the modulation frequency was collected with the aid of a digital lock-in amplifier (Stanford Research Systems SR830).

Ferroelectric hysteresis in mesoscopic (about $20 \mu\text{m}$ thick) KBNNO film samples ($x = 0.1$) was carried out at $77\text{--}200 \text{ K}$ under 10^{-7} torr and at 300 K under ambient pressure in a probe station (Lakeshore Desert Cryotronics TTP4) using a ferroelectric tester (model LC, Radiant Technologies) and a high-voltage amplifier with selected bias voltage sweep rate periods ranging from 10 ms to 10 s and selected peak voltages of up to 500 V , and poling using direct-current bias for different durations ranging from 5 s to 400 s .

Photocurrent and Raman measurements. Electrical contacts were produced on KBNNO samples and BaTiO_3 samples using a shadow mask and Cr/Au layers, and on mesoscopic (about $20 \mu\text{m}$ thick) and polished films using thermally evaporated $200 \mu\text{m} \times 200 \mu\text{m}$ Cr–Au (bottom side) and ITO deposited by pulsed laser deposition at 200°C using shadow masks. The resulting structures on bulk were $85 \mu\text{m} \times 85 \mu\text{m}$ pads separated by $45\text{-}\mu\text{m}$ gaps. Steady-state photocurrent/bias-voltage traces were collected under a halogen spectrally broad lamp probe illuminator (Dolan-Jenner MI-150), and alternately using a broadband supercontinuum laser source (NKT Compact) under ambient pressure and vacuum (10^{-7} torr, Lakeshore Cryotronics Model TTP4) using a picoammeter (Keithley model 6487). Photocurrent spectra were collected over the range of 700 nm to 900 nm using a wavelength-tunable Ti:sapphire laser (M2 SolsTiS). The laser radiation incident on the sample was about 10 mm in diameter, resulting in an incident intensity of 120 mW cm^{-2} . The laser spot was directed on the sample and aligned by maximizing the resulting output current. The BaTiO_3 photocurrent measurements were carried out on (100)-oriented substrate-grade BaTiO_3 (MTI Corporation). Raman scattering was collected at 300 K using the 543.5-nm laser line (Horiba Jobin-Yvon). Raman spectra were collected at 300 K under ambient pressure from a $x = 0.1\text{--}0.4$ bulk KBNNO sample and from KBNbO_3 .

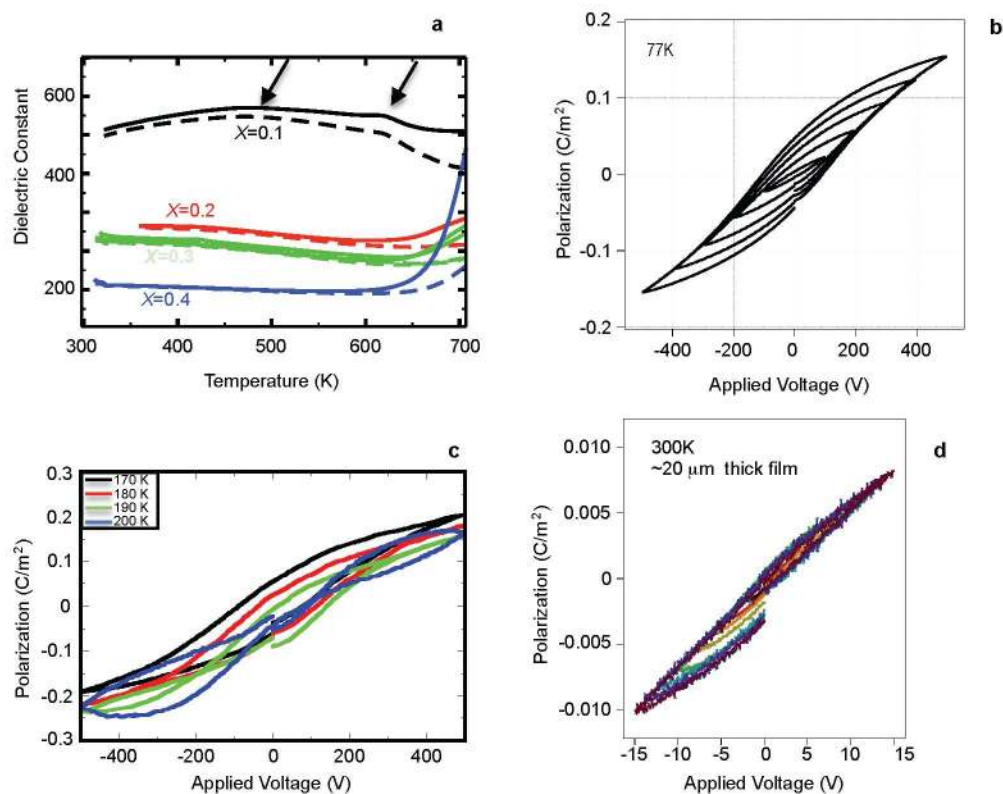
Computational modelling. We perform first-principles calculations with a plane-wave basis set, as implemented in Quantum-Espresso³². The LDA exchange-correlation functional is used for structural relaxations, with a $6 \times 6 \times 6$ Monkhorst–Pack k -point grid and a 50-Ry plane-wave cut-off. All atoms are represented by norm-conserving optimized nonlocal pseudopotentials, generated with the OPIUM code (<http://opium.sourceforge.net>). The electronic contribution to the polarization is calculated following the Berry's phase formalism.

Because LDA severely underestimates the bandgap, and even falsely predicts KBNNO to be metallic, all the electronic structure calculations have been done at the level of LDA + U . Although LDA + U is unable to predict E_g with the accuracy of the more advanced hybrid functionals or GW³³ methods, it can still provide a good description of the change of E_g with respect to the solid-solution cation ordering¹⁷. A simplified version of the rotationally invariant formulation of the LDA + U method is employed in the present work, where U can be determined by self-consistent linear-response calculations. Under the conditions of our synthesis, LDA + U free-energy calculations²³ show oxygen vacancies to be thermodynamically favoured.

The dependence of bandgap on composition is due to the interplay between local bonding and the bandgap in KBNNO, as elucidated by LDA + U calculations. There are two possible configurations for the oxygen vacancies in KBNNO, $\text{Ni-V}_\text{O}\text{--Ni}$ and $\text{Ni-V}_\text{O}\text{--Nb}$. Our calculations show that although both $\text{Ni-V}_\text{O}\text{--Ni}$ and $\text{Ni-V}_\text{O}\text{--Nb}$ configurations result in a lower bandgap owing to the introduction of the Ni $3d$ states, an extra density-of-states peak, contributed by the d -orbitals of the six-fold-coordinated Ni, is present in the valence-band maximum in $\text{Ni-V}_\text{O}\text{--Nb}$ (see Supplementary Fig. 3). Therefore the E_g of the $\text{Ni-V}_\text{O}\text{--Nb}$ configuration is lower than that of the $\text{Ni-V}_\text{O}\text{--Ni}$ configuration. This configuration is also found to be more energetically favourable for our calculations. At low BNNO concentration, the Ni cations are isolated, so the $\text{Ni-V}_\text{O}\text{--Nb}$ arrangement is prevalent. As Ni concentration increases, more $\text{Ni-V}_\text{O}\text{--Ni}$ configurations are formed and therefore the measured bandgap E_g rises.

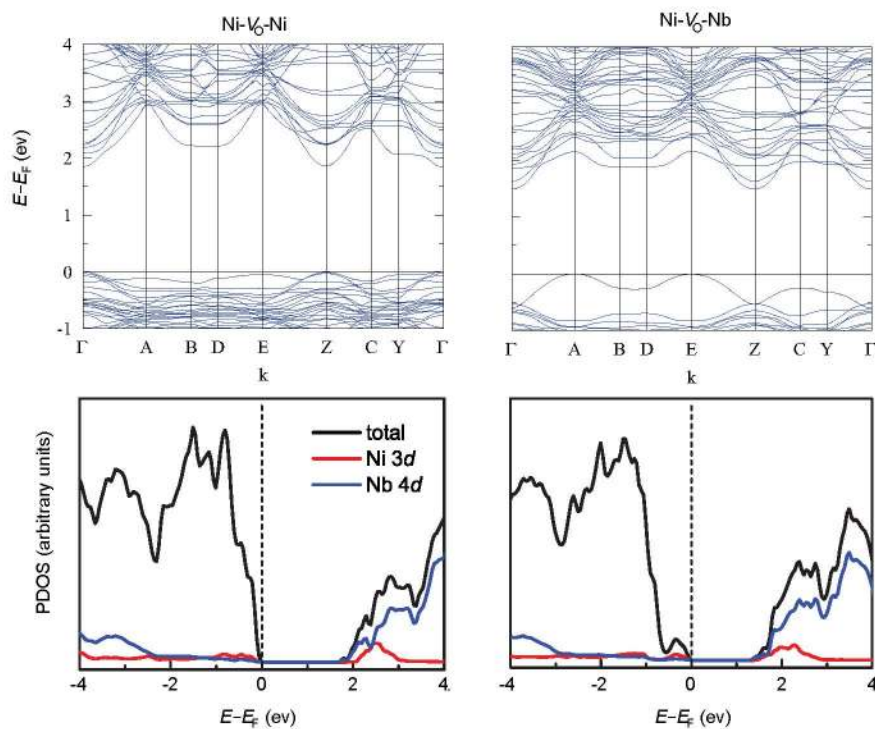
32. Giannozzi, P. *et al.* QUANTUM ESPRESSO: a modular and open-source software project for quantum simulations of materials. *J. Phys. Condens. Matter* **21**, 395502 (2009).

33. Hybertsen, M. S. & Louie, S. G. Electron correlation in semiconductors and insulators: band gaps and quasiparticle energies. *Phys. Rev. B* **34**, 5390–5413 (1986).



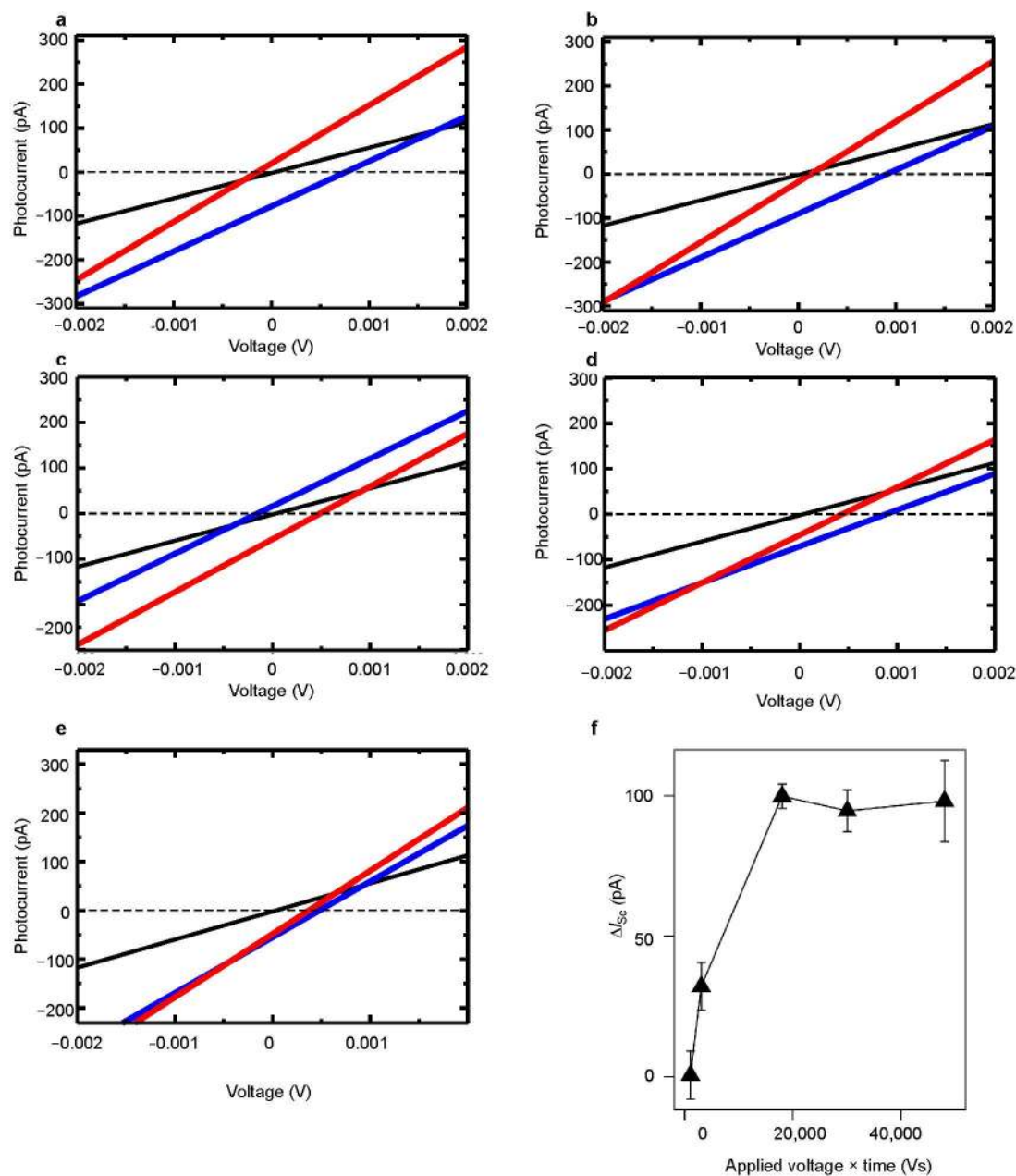
Extended Data Figure 1 | Ferroelectric and dielectric data. **a**, Dielectric data for $x = 0.1$ – 0.4 KBNNO. Two dielectric anomalies (arrows) at about 450 K and about 600 K are present (solid lines indicate heating; dotted lines indicate cooling). **b**, Ferroelectric hysteresis loops at 77 K, showing the effect of

increasing the maximum poling voltage. **c**, Ferroelectric hysteresis loop for approximately $20\text{-}\mu\text{m}$ -thick $x = 0.1$ KBNNO film at 170–200 K. **d**, Ferroelectric hysteresis loop for approximately $20\text{-}\mu\text{m}$ -thick $x = 0.1$ KBNNO film at 300 K.



Extended Data Figure 2 | Electronic Structure of KBNNO. Band structures (top) and orbital-projected density of states (PDOS, bottom) for KBNNO $\text{Ni-V}_\text{O}\text{-Ni}$ and $\text{Ni-V}_\text{O}\text{-Nb}$ solid solutions near the Fermi level. The high-symmetry points in the Brillouin zone are Γ (0, 0, 0) A (−0.5, 0.5, 0),

B (−0.5, 0, 0), D (−0.5, 0, 0.5), E (−0.5, 0.5, 0.5), Z (0, 0, 0.5), C (0, 0.5, 0.5) and Y (0, 0.5, 0). k is the wavevector. The more stable $\text{Ni-V}_\text{O}\text{-Nb}$ structure provides a smaller bandgap. As Ni concentration rises, $\text{Ni-V}_\text{O}\text{-Ni}$ becomes more common and the bandgap energy rises.



Extended Data Figure 3 | Switchable bulk photovoltaic effect in KBNNO and the dependence of photocurrent on poling. Ferroelectric photovoltaic effect for approximately 20- μm -thick $x = 0.1$ KBNNO film in ambient conditions under 4 mW cm^{-2} of above-bandgap illumination following poling by an 80-V pulse applied for 300 s (a), a 50-V pulse applied for 300 s (b), a 50-V pulse applied for 180 s (c), a 50-V pulse applied for 30 s (d) and a 50-V pulse applied for 10 s under 4 mW cm^{-2} of above-bandgap illumination (e). Black denotes collected dark current; blue and red traces indicate photocurrent following poling under positive and negative voltages, respectively. f, Short-circuit photocurrent I_{sc} for different product of duration and magnitude of poling voltage. The current is collected through

200 $\mu\text{m} \times 200 \mu\text{m}$ ITO and Cr-Au electrodes on the top and bottom of the sample, respectively. The height of each error bar is two standard deviations in the measured short-circuit current. As the applied voltage and poling time are increased, the difference between the photocurrents for the up- and down-polarized sample increases and the photocurrent magnitude rises by two orders of magnitude until saturation caused by leakage. This indicates that the sample is not yet fully poled even for the highest voltage possible in our set-up. Therefore, our results are the lower limit for the photocurrent for a fully poled material that can be achieved by application of larger electric fields in thinner films.

Extended Data Table 1 | Comparison of structural data from experiment and DFT calculations

		<i>a</i> (Å)	<i>V</i> (Å ³)
DFT	KNbO ₃	3.985	63.26
	0.33 KBNNO Ni-Vac-Ni	3.986	63.35
	0.33 KBNNO Ni-Vac-Nb	3.99	63.64
	0.33 KBNNO Ni-O-Ni	3.975	62.86
	0.33 KBNNO Ni-O-Nb	3.971	62.59
Experiment	KNbO ₃	4.015	64.70
	0.3 KBNNO	4.036	65.74

Pseudo-cubic lattice constant *a* and volume *V* values are as obtained computationally by DFT–LDA relaxations and by experimental X-ray diffraction measurements. DFT calculations for KBNNO with vacancies correctly reproduce the experimentally observed increase in the cell volume with increased BNNO content. In contrast, fully oxidized KBNNO samples show a decrease in cell volume compared to the parent KNbO₃ material. This indicates that the experimentally studied material is indeed KBNNO with vacancies.